

Linear single-step image reconstruction in the presence of nonscattering regions

H. Dehghani* and D. T. Delpy

Department of Medical Physics and Bioengineering, University College London, 11-20 Capper Street, London WC1E 6JA, UK

Received July 25, 2001; revised manuscript received October 25, 2001; accepted November 5, 2001

There is growing interest in the use of near-infrared spectroscopy for the noninvasive determination of the oxygenation level within biological tissue. Stemming from this application, there has been further research in using this technique for obtaining tomographic images of the neonatal head, with the view of determining the level of oxygenated and deoxygenated blood within the brain. Because of computational complexity, methods used for numerical modeling of photon transfer within tissue have usually been limited to the diffusion approximation of the Boltzmann transport equation. The diffusion approximation, however, is not valid in regions of low scatter, such as the cerebrospinal fluid. Methods have been proposed for dealing with nonscattering regions within diffusing materials through the use of a radiosity-diffusion model. Currently, this new model assumes prior knowledge of the void region; therefore it is instructive to examine the errors introduced in applying a simple diffusion-based reconstruction scheme in cases where a nonscattering region exists. We present reconstructed images, using linear algorithms, of models that contain a nonscattering region within a diffusing material. The forward data are calculated by using the radiosity-diffusion model, and the inverse problem is solved by using either the radiosity-diffusion model or the diffusion-only model. When using data from a model containing a clear layer and reconstructing with the correct model, one can reconstruct the anomaly, but the qualitative accuracy and the position of the reconstructed anomaly depend on the size and the position of the clear regions. If the inverse model has no information about the clear regions (i.e., it is a purely diffusing model), an anomaly can be reconstructed, but the resulting image has very poor qualitative accuracy and poor localization of the anomaly. The errors in quantitative and localization accuracies depend on the size and location of the clear regions. © 2002 Optical Society of America

OCIS codes: 0170.3660, 100.3010.

1. INTRODUCTION

Optical tomography is a noninvasive imaging technique that aims to image the optical properties of biological tissue, particularly the peripheral muscle, the breast, and the brain.^{1–12} An optode placed on the surface of the region of interest will deliver an input optical signal (either continuous, amplitude-modulated, or ultrashort pulses), while other optodes placed at different locations on the same surface will detect the outgoing photons that have propagated through the volume under investigation. The intensity and the path-length distribution of the exiting photons provide information about the optical properties of the transilluminated tissue. This information, the so-called boundary data, can be used to reconstruct images of the distributions of internal absorption μ_a and reduced scattering coefficient μ'_s .

Numerical modeling of light propagation in scattering tissue has become well established in optical tomography largely through the use of the diffusion approximation to the Boltzmann transport equation.^{13–15} The diffusion approximation is, however, valid only for materials that are much more scattering than absorbing ($\mu'_s \gg \mu_a$). This may be suitable for measurements involving largely scattering media; for example, the female breast or the peripheral muscle. Our major interest in optical tomography, however, lies in its use for the imaging of the neonatal head. In such studies, the aim would be to detect changes in the oxygenation state of specific regions of the brain as an aid to the understanding and the prevention

of cerebral handicap.¹⁶ Within the head, there are regions that are nonscattering while still absorbing, namely, the cerebrospinal fluid (CSF) layer around the brain and in the ventricles. The presence of CSF prevents the accurate modeling of photon propagation within the regions of interest when using the diffusion approximation.^{17–24}

In previous publications, we introduced the concept of the modeling of domains that contain clear nonscattering void regions by the use of the radiosity-diffusion model.^{18,19} In those studies, we showed that given a scattering domain that contains nonscattering void regions, we can model the propagation of light through this region by applying the diffusion approximation in scattering regions and the radiosity theory in nonscattering regions through the use of a hybrid method. In a following paper,²⁰ we showed that the nonlinear reconstruction of the μ_a distribution from a model containing nonscattering void regions fails if no *a priori* information regarding the nonscattering regions is used.

Another form of imaging is dynamic imaging, where one is looking for changes in data measured at two different states or over a period of time. This change in data is then used to reconstruct images of changes in either μ_a or μ'_s . Any change in optical parameters must be regarded as small, so that the change in measured data can be assumed to be linear. Linear image reconstruction allows the precomputation of the reconstruction algorithm based on some assumed distribution of optical properties, from

which deviations of optical parameters are imaged. This permits a fast and robust reconstruction algorithm, with its accuracy dependent on the correct modeling and the regularization method used.²⁵

A recent study has shown that under linear diffuse assumptions, images of changes in optical properties can be reconstructed by using data from a domain containing clear nonscattering void regions.²⁶ It is important to know whether the use of linear algorithms produces accurate and dependable results in these circumstances. In the present study, we therefore investigated the effect of the presence of relatively simple nonscattering regions upon absorption-only images reconstructed by using a diffusion-based model, in particular simulating the case of the CSF-filled regions within the neonatal head.

As an overview of the paper, we will present the case of linear image reconstruction for a purely diffusing model and will then extend this model to contain a clear layer of varying thickness as well as void regions deep within the model to simulate the presence of ventricles within the neonatal head. The reconstruction algorithm used is such that in a clinical environment, the images will be reconstructed from measured data with reference to previous measurements taken before a change has occurred, for example, over a period of time where one is looking for dynamic changes in absorption due to a stimulus or a condition.

2. METHOD AND RESULTS

In accordance with Refs. 13, 14, and 18, we have used the finite element method for the calculation of light propagation in a model, employing either the diffusion approximation or the radiosity-diffusion model. The finite element method model based on the diffusion approximation is used for the modeling of light transport in purely diffusing material, whereas the radiosity-diffusion model has been used to calculate light propagation in diffusing models containing one or more nonscattering void regions.

We assume that a change in measured data, from \mathbf{y}_0 to \mathbf{y}_1 , either intensity or mean time, due to a small change in internal absorption at position r , from $\mu_{a0}(r)$ to $\mu_{a1}(r)$, is represented by a linear operator:

$$\mathbf{y}_1^{\mathcal{M}} - \mathbf{y}_0^{\mathcal{M}} = \mathcal{J}^{\mathcal{M}}[\mu_{a1}(r) - \mu_{a0}(r)], \quad (1)$$

where \mathcal{M} represents a measurement type.²⁷ \mathcal{J} is known as the Jacobian, or the sensitivity function, and it gives the relationship between a small change in data due to a small change in an internal optical property (in this work, μ_a). To calculate the change in absorption from a change in measured data, we solve Eq. (1) by using the generalized inverse method.²⁵

$$\mu_{a1}(r) - \mu_{a0}(r) = \mathcal{J}^T(\mathcal{J}\mathcal{J}^T)^{-1}(\mathbf{y}_1^{\mathcal{M}} - \mathbf{y}_0^{\mathcal{M}}). \quad (2)$$

However, the square matrix $\mathcal{J}\mathcal{J}^T$ is ill posed and near singular. To calculate an approximate inverse, we need to either regularize this square matrix or use the truncated singular value decomposition method.²⁸ In this work, we have used the latter method, since the truncation level of the singular values can be easily calculated for the amount of noise expected in the measured data.

In the following examples, several different forward models are used to generate data. In each case, a two-dimensional circular model of radius 35 mm is used, with 16 sources and detectors placed equidistant on the outer boundary. The sources were modeled as point sources, and a Robin boundary condition was used.¹⁴

To look at the effect of a clear layer on the reconstruction of internal μ_a changes, we investigate various cases. Initially, we will show images reconstructed when the data (either intensity or meantime) are calculated for a purely diffusing model and the Jacobian \mathcal{J} is also calculated from the same diffusing model. Then, we will present images where the data are calculated from a model that contains a clear region and \mathcal{J} is calculated either from the forward model used for the generation of forward data or from a purely diffusing model.

The exact characteristics of the models, including the mesh sizes, the numbers of sources and detectors, the source model, and the number of singular values used, were made, as far as possible, identical. In each case, only μ_a images are considered, and images are reconstructed from data with 1% added noise. A general outline of the models used in the following is shown in Fig. 1.

A. Case 1: Purely Diffusing Model

The first case considered is a purely diffusing model. The background optical properties of the diffusing region were set as $\mu'_s = 1 \text{ mm}^{-1}$ and $\mu_a = 0.01 \text{ mm}^{-1}$ with a refractive index of 1.4. A Gaussian anomaly of full width at half-maximum 2 mm was placed 18.4 mm from the center of the model. The anomaly had the same scattering and refractive-index properties as those of the background and a peak absorption value of $\mu_a = 0.05 \text{ mm}^{-1}$.

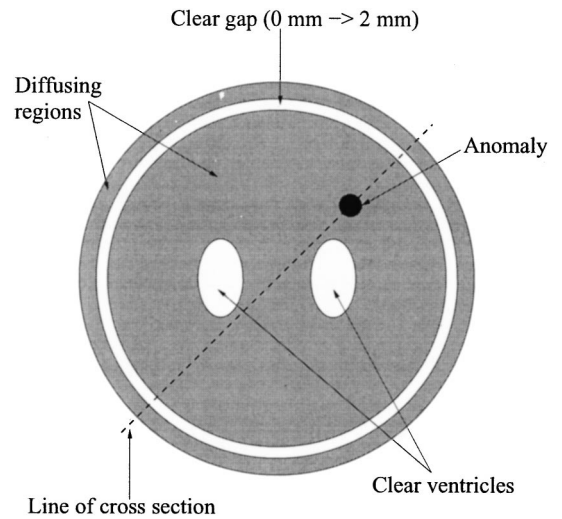


Fig. 1. Outline of the models used to generate the forward data as well as the image reconstruction. The background optical properties of the diffusing region were set as $\mu'_s = 1 \text{ mm}^{-1}$ and $\mu_a = 0.01 \text{ mm}^{-1}$ with a refractive index of 1.4. The nonscattering regions had an absorption value of $\mu_a = 0.005 \text{ mm}^{-1}$ and a refractive index of 1.4. A Gaussian anomaly of full width at half-maximum 2 mm was placed 18.4 mm from the center of the model. The anomaly had the same scattering and refractive-index properties as those of the background and a peak absorption value of $\mu_a = 0.05 \text{ mm}^{-1}$. The dotted line indicates the axis along which μ_a profiles are plotted in Figs. 9, 10, and 12 below.

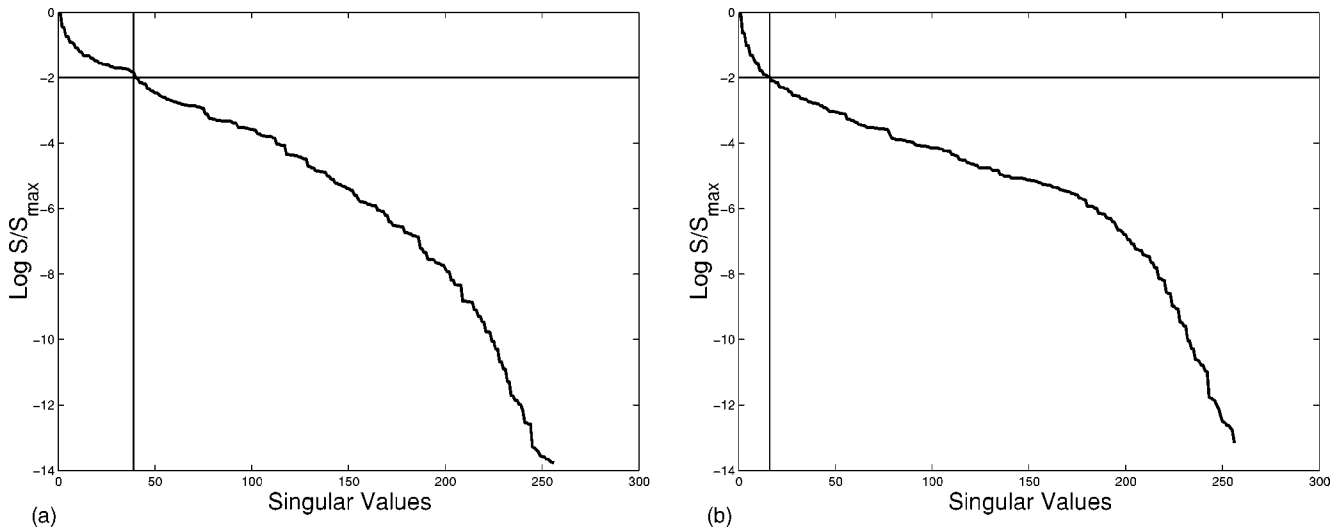


Fig. 2. Singular values (a) Jacobian for intensity and μ_a and (b) Jacobian for mean time and μ_a , calculated for the purely diffusing model. The intersection of the straight lines shows the position of the truncation used.

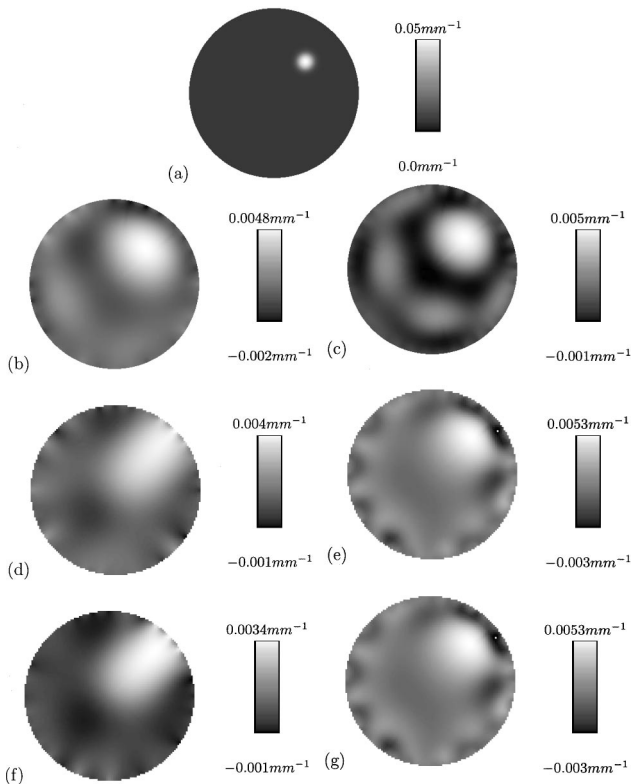


Fig. 3. Diffusion-only model. (a) Target image μ_a difference images reconstructed from (b) intensity and (c) mean-time data. Images reconstructed by normalizing the data with the reference measurement for (d) intensity and (e) mean-time data. Images reconstructed by normalizing the data with the rms of the reference measurement for (f) intensity and (g) mean-time data.

To reconstruct images of μ_a changes, the Jacobians for intensity and mean-time data were calculated²⁹ for the same model as that used to generate the data, using the background homogeneous values of $\mu'_s = 1 \text{ mm}^{-1}$ and $\mu_a = 0.01 \text{ mm}^{-1}$. Next, the singular value decomposi-

tion for the square matrix JJ^T was calculated (shown in Fig. 2). In this figure, the log of singular values, normalized to the first (and largest) singular value, is plotted against the total number of singular values (256, 16 sources \times 16 detectors). Since the data have 1% added noise, the level of truncation used corresponds to the singular values that are equal to or greater than 1% of the largest singular value. For the two Jacobians shown in Fig. 2, this corresponds to 39 for the intensity case and 16 for the mean-time case. Images were reconstructed, and the results are shown in Fig. 3.

In Fig. 3(a), the target image is shown, and in Figs. 3(b) and 3(c), the μ_a difference images reconstructed from the difference in intensity and mean-time data (with and without anomaly present) are shown, respectively. The peak μ_a value for the anomaly calculated by using intensity data is 0.0048 mm^{-1} , and that with mean-time data is 0.006 mm^{-1} . The position of the reconstructed anomaly (calculated as the location of the peak value) is 19.24 mm from the center when using either intensity or mean-time data. It is important to note that the absolute amplitudes of the reconstructed anomalies are small compared with the target. If more singular values are considered in the inversion of the Jacobian matrix, the quantification of the reconstruction improves at the expense of more high-frequency noise in the image.

In addition, to review other variations of single-step reconstruction using the described method, we have also used normalized data for the reconstruction. Normalized data can be used to compensate for the large dynamic range in data (for example, intensity data, where the data collected near the source are much larger than the data collected at furthest distance) and to compensate for any errors or artifacts that may be contained in the measured data. We have used two types of normalization: (1) that using the reference measurement and (2) that using the root mean square (rms) of the reference measurement. Reconstructed images can be seen in Figs. 3(d) and 3(e) for the normalization using the reference data themselves and in Figs. 3(f) and 3(g) for the normalization using the rms of the reference data. As is evident, the original

data seem to produce the best quality of difference images of μ_a ; therefore, for the remainder of this work, we will use the unnormalized difference in data.

B. Case 2: 1-mm-Gap Model

The next model contains a 1-mm nonscattering ring placed 3 mm from the outer boundary. The background optical properties of the diffusing region were the same as those case 1. The nonscattering ring had an absorption value of $\mu_a = 0.005 \text{ mm}^{-1}$ and a refractive index of 1.4. The Gaussian anomaly was the same as that in case 1.

As in the above case, the Jacobians for both intensity and mean-time data were calculated for the same model as that used to generate the forward data, and the corresponding singular values for the square matrix JJ^T were calculated. The truncation level used for these matrices corresponds to 39 for the intensity case and 17 for the mean-time case.

In Fig. 4(a), the target image is shown, and in Figs. 4(b) and 4(c), the μ_a difference images reconstructed from the difference in intensity and mean-time data (with and without anomaly present) are shown, respectively. The peak value calculated by using both intensity and mean-time data is 0.0024 mm^{-1} . The position of the reconstructed anomaly is 19.4 mm from the center when using the intensity data and 20.1 mm from the center when using the mean-time data.

To simulate the effect on the image if no *a priori* knowledge is known, we have also reconstructed images by using the Jacobian from case 1. The resulting images, Figs. 4(d) and 4(e), show the difference images using the difference in intensity and mean-time data. The peak value calculated by using intensity data is 0.0036 mm^{-1} , and that with mean-time data is 0.0077 mm^{-1} . The position of the reconstructed anomaly is 17.5 mm from the center when using the intensity data and 15.75 mm from the center when using the mean-time data.

C. Case 3: 2-mm-Gap Model

This model is similar to case 2, but with a 2-mm nonscattering ring placed 3 mm from the outer boundary. The background optical properties of the diffusing region and the nonscattering ring were the same as those in case 2. The Gaussian anomaly was the same as that above.

As in the above cases, the Jacobians for intensity and mean-time data were calculated for the same model as that used to generate the data, and the corresponding singular values for the square matrix JJ^T were calculated. The truncation level used for these matrices corresponds to 36 for the intensity case and 12 for the mean-time case. Images were again reconstructed by using intensity and mean-time data (Fig. 5). The peak value calculated by using intensity data is 0.0012 mm^{-1} , and that with mean-time data is 0.0017 mm^{-1} . The position of the reconstructed anomaly is 22.8 mm from the center when using the intensity data and 22.5 mm from the center when using the mean-time data.

The effect of reconstruction using the Jacobian from the purely diffusing case, i.e., where no *a priori* knowledge is assumed, is shown in Figs. 5(d) and 5(e). The peak value calculated by using intensity data is 0.001 mm^{-1} , and that with mean-time data, is 0.0038 mm^{-1} .

The position of the reconstructed anomaly is 10 mm from the center when using the intensity data and 5.2 mm from the center when using the mean-time data.

D. Case 4: Irregular-Gap Thickness

In the above models, the clear layer had a smooth boundary, and its presence had a significant effect on the reconstructed images. In reality, the CSF layer around the brain is irregular, and it has been suggested³⁰ that the profound effect of the smooth clear layer investigated above is due to the extended "line of sight" for the photons

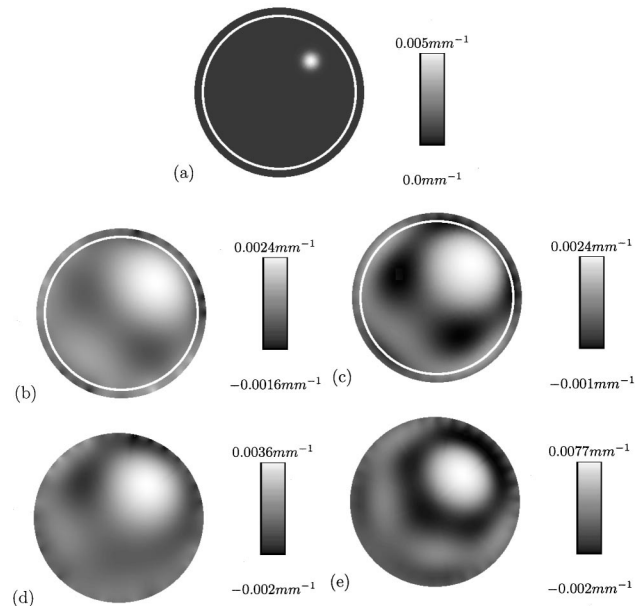


Fig. 4. Diffusing model with a 1-mm-thick nonscattering ring placed 3 mm from the outer boundary. (a) Target image μ_a difference images from (b) intensity and (c) mean-time data and the correct Jacobian μ_a difference images from (d) intensity and (e) mean-time data but using the diffusion-only Jacobian.

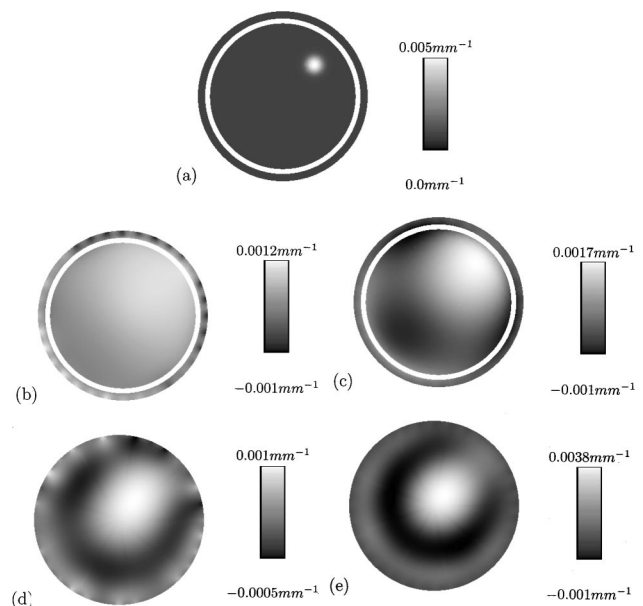


Fig. 5. Same as Fig. 4 but with a 2-mm-thick nonscattering ring placed 3 mm from the outer boundary.

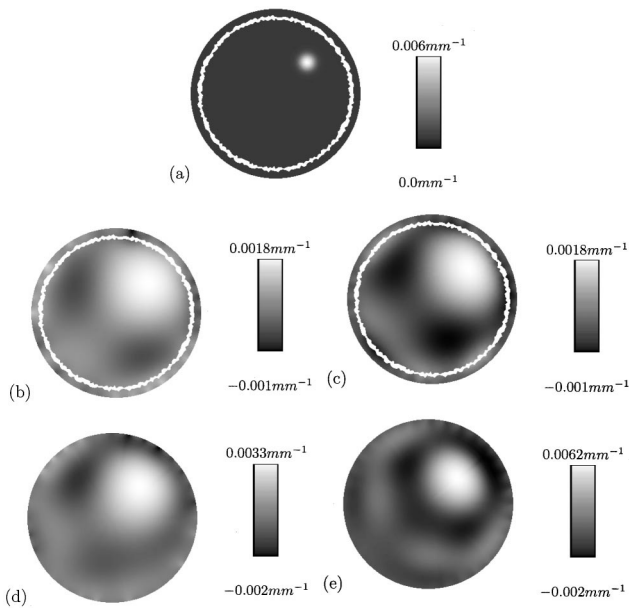


Fig. 6. Diffusing model with an irregular nonscattering ring placed 3 mm from the outer boundary. (a) Target image μ_a difference images from (b) intensity and (c) mean-time data and the correct Jacobian μ_a difference images from (d) intensity and (e) mean-time data but using the diffusion-only Jacobian.

crossing this region, which would be more limited if the boundary were irregular. A model with an irregular bounded gap was therefore simulated to examine this effect. The irregular boundary was calculated by adding noise to the x and y coordinates of the smooth boundary and then smoothing to a desired level by removing the higher-frequency roughness. In this model, the maximum thickness of the nonscattering ring is 2.5 mm and the minimum is approximately 0.5 mm, with a mean of 1.507 mm. The average was calculated by taking the mean of the radial distance across the clear layer for each degree of rotation around the model. The optical properties were the same as those in the above cases, as were the details of the anomaly.

As above, the Jacobians for intensity and mean-time data were calculated by using this same model, and the corresponding singular values for the square matrix JJ^T were calculated. The truncation level used for these matrices corresponds to 37 for the intensity case and 17 for the mean-time case. Images were reconstructed, and the results are shown in Fig. 6. The peak value calculated by using intensity data is 0.0018 mm^{-1} , and that with mean-time data is 0.0018 mm^{-1} . The position of the reconstructed anomaly is 18.2 mm from the center when using the intensity data and 19 mm from the center when using the mean-time data.

Figures 6(d) and 6(e) show the difference images calculated by using the Jacobian from the purely diffusing model, i.e., assuming no *a priori* information. The peak value calculated by using intensity data is 0.0033 mm^{-1} , and that with mean-time data is 0.0062 mm^{-1} . The position of the reconstructed anomaly is 17.5 mm from the center when using the intensity data and 15.7 mm from the center when using the mean-time data.

E. Case 5: 1- and 2-mm-Gap Models with Ventricles

In addition to a layer of clear CSF around the brain, the real head contains other nonscattering regions, the ventricles. To examine the effects of their presence, we modified the models used in cases 2 and 3 to include oval-shaped ventricles placed deep within the model [Figs. 7(a) and 8(a)]. The ventricles were oval shaped and centered 10 mm on either side of the model's origin. They had major and minor axes of 7 and 4 mm, respectively. The optical properties were the same as those in the above cases, as were the details of the anomaly.

Again, the Jacobians for intensity and mean-time data were calculated for this model, and the corresponding singular values for the square matrix JJ^T were calculated. The truncation level used for these matrices corresponds to 40 (for the 1-mm model with ventricles) and 38 (for the 2-mm model with ventricles) for the intensity case and to 17 (both models) for the mean-time case. Images were reconstructed, and the results shown in Figs. 7 and 8.

For the 1-mm model with ventricles, the peak value calculated by using intensity data is 0.0023 mm^{-1} , and that with mean-time data is 0.0016 mm^{-1} . The position of the reconstructed anomaly is 19.4 mm from the center when using the intensity data and 21.2 mm from the center when using the mean-time data. For the 2-mm model with ventricles, the peak value calculated by using intensity data is 0.001 mm^{-1} , and that with mean-time data is 0.0016 mm^{-1} . The position of the reconstructed anomaly is 18 mm from the center when using the intensity data and 23.6 mm from the center when using the mean-time data.

Figures 7 and 8(d)–8(e) show the difference images calculated by using the Jacobian from the purely diffusing

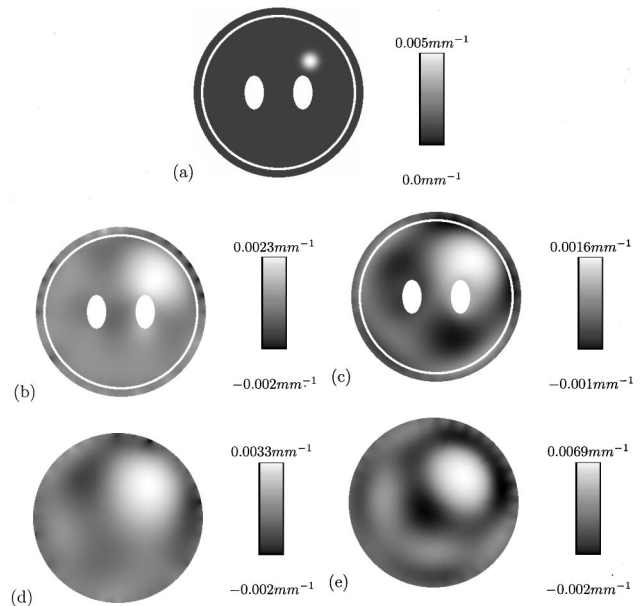


Fig. 7. Diffusing model with a 1-mm-thick nonscattering ring placed 3 mm from the outer boundary. Also, there are two nonscattering ellipse-shaped regions, with a major axis of 7 mm and a minor axis of 4 mm, centered 10 mm on either side of the model origin. (a) Target image μ_a difference images from (b) intensity and (c) mean-time data and the correct Jacobian μ_a difference images from (d) intensity and (e) mean-time data but using the diffusion-only Jacobian.

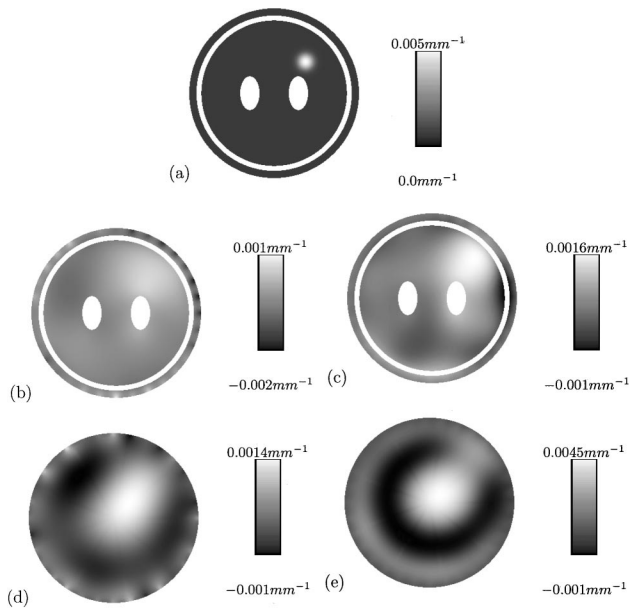


Fig. 8. Same as Fig. 7 but with a 2-mm-thick nonscattering ring placed 3 mm from the outer boundary.

model. For the 1-mm model with ventricles, the peak value calculated by using intensity data is 0.0033 mm^{-1} , and that with mean-time data is 0.0069 mm^{-1} . The position of the reconstructed anomaly is 17.5 mm from the center when using the intensity data and 15.7 mm from the center when using the mean-time data. For the 2-mm model with ventricles, the peak value calculated by using intensity data is 0.0014 mm^{-1} , and that with mean-time data is 0.0045 mm^{-1} . The position of the reconstructed anomaly is 8.7 mm from the center when using the intensity data and 5.2 mm from the center when using the mean-time data.

To analyze these results in more detail, cross-section plots (as shown in Fig. 1) of the calculated μ_a difference for each model, as well as the target distribution, are shown in Figs. 9 and 10 for intensity and mean-time data, respectively.

Figure 9(a) shows the cross section through the images, calculated by using intensity difference data and with the correct Jacobian for each model. It can be seen from this plot that although the qualitative value for all the μ_a difference in the reconstructions is not correct, the anomaly is reconstructed at approximately the correct position and that the degree of broadening of the anomaly is dependent on the width of the nonscattering gap. The most successful reconstruction is obtained for the purely diffusing model. Once a clear gap is introduced, the quantitative value of the reconstructed μ_a is reduced. It is of interest to note that the irregular-gap model demonstrates a better performance than that of the corresponding model with a 2-mm-wide smooth-surfaced clear ring, and indeed the reconstruction is as good as that obtained with the 1-mm-thick clear ring. It can also be seen that the 2-mm-gap model with ventricles rather surprisingly gives a slightly better reconstruction than that using the 2-mm-gap model without ventricles. The reason for this can be found by looking at the Jacobians (Fig. 11), where it is ap-

parent that the presence of the ventricles in the model have increased the sensitivity for this region, where the anomaly is placed.

Figure 9(b) is the equivalent plot of the cross section through the image reconstructed by using intensity difference data but this time using the Jacobian for the purely diffusing model. Again, we can see that the anomaly is reconstructed at approximately the correct position for the 1-mm-gap models and the irregular-gap model. However, as soon as the gap thickness is increased to 2 mm, not only does the reconstructed image show extensive blurring, but also the anomaly is reconstructed at the wrong location (taken as the peak of the curve).

Figure 10(a) is the cross-section plot through the images, reconstructed by using mean-time difference data with the correct Jacobian for the model. It can be seen from this plot that although the qualitative values are not correct, the anomaly is reconstructed at approximately the correct position, and the degree of broadening is dependent on the size of the gap. Once more, the reconstruction is more successful for the purely diffusing model with no clear gap. Once a clear gap is introduced, the

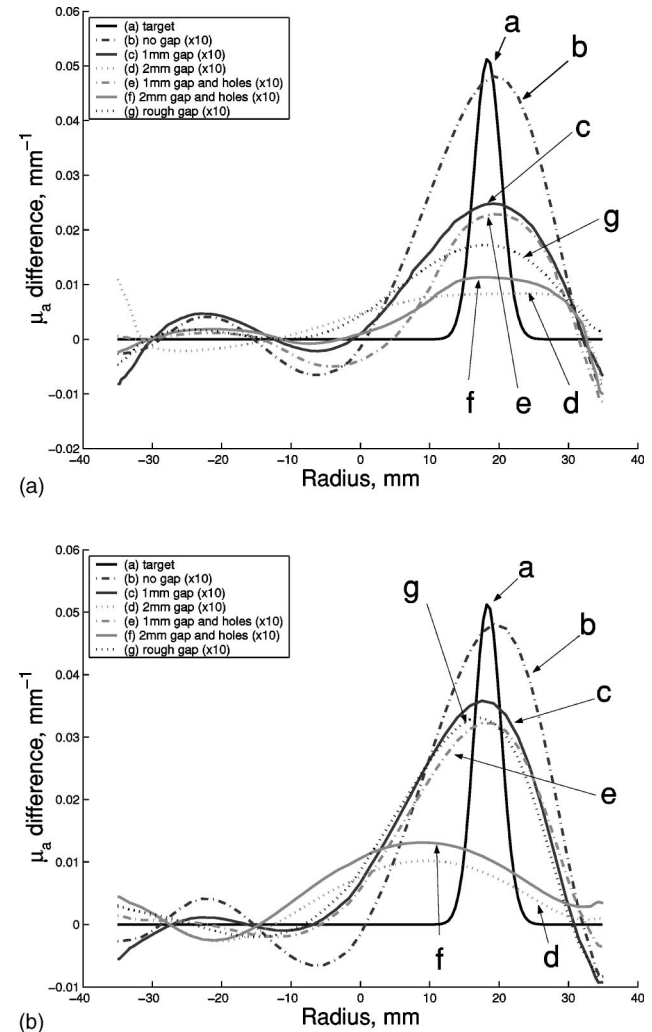


Fig. 9. Cross-section plots through each reconstruction along the line indicated in Fig. 1 using the intensity difference data and (a) the correct Jacobian or (b) a Jacobian calculated assuming a purely diffusing model.

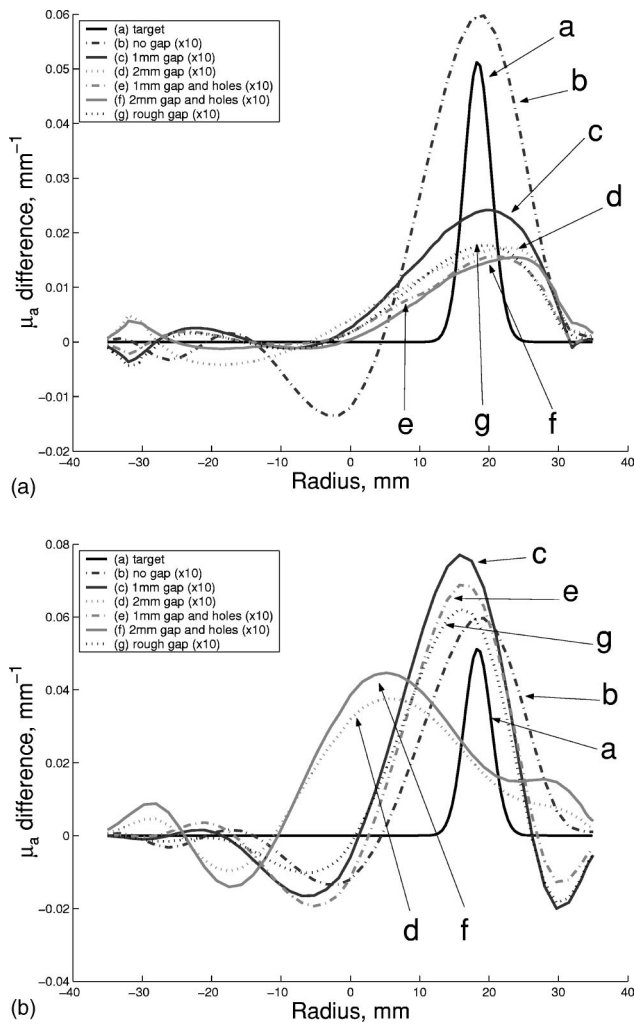


Fig. 10. Same as Fig. 9 but using the mean-time difference data.

quantitative μ_a values of the reconstruction are reduced. It is of interest to note that the irregular-gap model again shows a performance better than that of the corresponding 2-mm-wide smooth-surfaced clear ring and almost as good as that of the 1-mm-thick clear ring. What is also noticeable is that for both the smooth 1- and 2-mm-gap models, the position of the reconstructed anomaly has shifted slightly toward the inner edge of the clear layer. This effect has been previously reported.²⁰

Figure 10(b) is the corresponding cross-section plot for the reconstruction using mean-time difference data with the Jacobian for the purely diffusing model. It can be seen from this plot that the anomaly is reconstructed at the correct position for only the purely diffusing model. As soon as a clear gap is introduced, the center of the anomaly is pushed toward the center of the model. This effect is greatest in the 2-mm-gap models. All of the above results are summarized in Tables 1 and 2.

F. Case 6: 2-mm-Gap Model with Ventricles Reconstructed with Varying Number of Singular Values

In all of the reconstructions shown so far, the inverse operator was calculated by using the inverse of the Jacobian. This inverse was calculated by taking the singular

value decomposition of the square matrix JJ^T , truncating the singular values at a desired point, and using this to calculate an approximate inverse to JJ^T . The level of truncation for each matrix was chosen such that the ratio of the largest singular value to the smallest singular value is no smaller than 1% (equal to the amount of noise in the data). The effect of using more singular values than this will result in sharper images at the expense of more noise and artifacts in the reconstruction, whereas if fewer singular values are used, the reconstructed image will be significantly smoother and more blurred.

We next investigated the effects of varying this truncation level when reconstructing images from a gap model but using a Jacobian from a purely diffusing model and mean-time data. The reason for doing this was to investigate if it is possible to improve the accuracy of this simple reconstruction, which requires no *a priori* information. The gap model used is the one with both a 2-mm gap and with ventricles, since this model showed the largest artifacts when reconstructing images using the Jacobian from the purely diffusing model. The inverse operator was calculated by using five different truncation levels

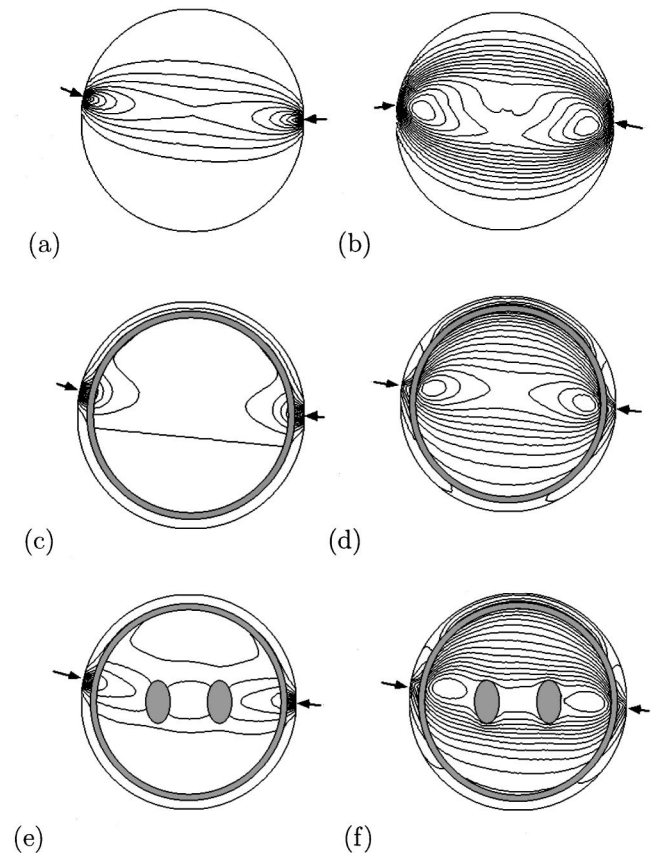


Fig. 11. Photon measurement density functions for the purely diffusing model [(a) μ_a distribution and intensity and (b) μ_a distribution and mean time], the 2-mm-gap case [(c) μ_a distribution and intensity and (d) μ_a distribution and mean time], and the 2 mm-gap case with holes [(e) μ_a distribution and intensity and (f) μ_a distribution and mean time]. The arrows show the position of source and detectors. The shaded regions in images (c)–(f) represent clear nonscattering regions. Each image contains 16 contour lines, each representing an equal percentage drop in sensitivity from a maximum (under the optodes) to a minimum.

Table 1. Reconstructed Parameters for Intensity Data

Forward Model	Inverse Model	Calculated μ_a (mm ⁻¹)	Calculated Position (mm)
Purely diffusing	Purely diffusing	0.0048	19.24
1-mm gap	1-mm gap	0.0024	19.4
2-mm gap	2-mm gap	0.0012	22.8
Irregular gap	Irregular gap	0.0018	18.2
1-mm gap with ventricles	1-mm gap with ventricles	0.0023	19.4
2-mm gap with ventricles	2-mm gap with ventricles	0.001	18
1-mm gap	Purely diffusing	0.0036	17.5
2-mm gap	Purely diffusing	0.001	10
Irregular gap	Purely diffusing	0.0033	17.5
1-mm gap with ventricles	Purely diffusing	0.0033	17.5
2-mm gap with ventricles	Purely diffusing	0.0014	8.7

Table 2. Reconstructed Parameters for Mean-Time Data

Forward Model	Inverse Model	Calculated μ_a (mm ⁻¹)	Calculated Position (mm)
Purely diffusing	Purely diffusing	0.006	19.24
1-mm gap	1-mm gap	0.0024	20.1
2-mm gap	2-mm gap	0.0017	22.5
Irregular gap	Irregular gap	0.0018	19
1-mm gap with ventricles	1-mm gap with ventricles	0.0016	21.2
2-mm gap with ventricles	2-mm gap with ventricles	0.0016	23.6
1-mm gap	Purely diffusing	0.0077	15.7
2-mm gap	Purely diffusing	0.0038	5.2
Irregular gap	Purely diffusing	0.0062	15.7
1-mm gap with ventricles	Purely diffusing	0.0069	15.7
2-mm gap with ventricles	Purely diffusing	0.0045	5.2

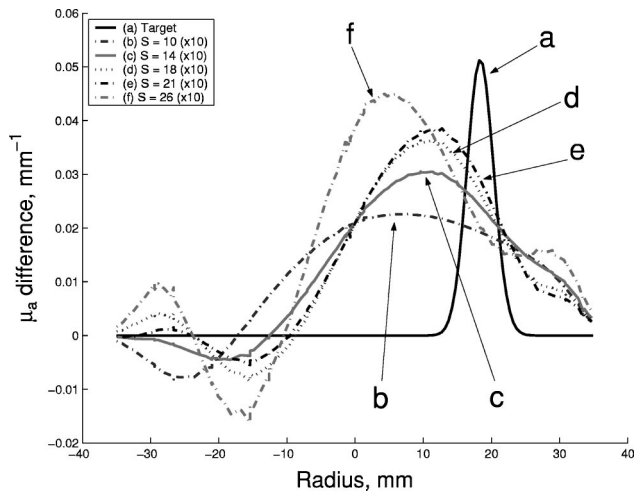


Fig. 12. Cross-section plots through each reconstruction along the line indicated in Fig. 1 using the mean-time difference data (from 2-mm-gap model with clear holes) and the Jacobian calculated assuming a purely diffusing model but with varying numbers of singular values (S) included in the reconstruction.

of 10, 14, 18, 21, and 26 singular values (compared with 16 in the purely diffusive case and 17 in the correct gap model). Images were reconstructed by using these, and the cross-section profiles of the resulting images are shown in Fig. 12.

From these images, it can be seen that, as expected, as the number of singular values included is reduced, the profile of the anomaly broadens. Also, as the number of

singular values is increased, it can be seen that the background μ_a in the image becomes less homogeneous (e.g., see the large dip at radius $x = 17$ mm). More significantly, it seems that when 14–21 singular values are used, the position of the reconstructed anomaly is shifted more toward its true position. When only ten singular values are used, the position is shifted toward the center of the model, which is what one would expect given the limited spatial-frequency information in these low singular values. However, a similar shift also seems to occur when a larger number of singular values is used (e.g., the data using 26 singular values). The image reconstructed by using 26 singular values is much sharper than that from ten singular values.

3. DISCUSSION AND CONCLUSIONS

Forward solutions of diffusion-based models that contain nonscattering regions have been calculated by using the radiosity-diffusion finite element method. Boundary data from these forward solutions were then used to reconstruct linearized images of the internal μ_a distribution with either a diffusion-only or a radiosity-diffusion model. In the radiosity-diffusion model, the position and the size of the nonscattering regions have to be known *a priori*.

In case 1, we showed the application of linear reconstruction when both the data and the inverse operator (inverse of the Jacobian) are calculated from a purely diffusing model. The reconstructions here showed the anomaly being reconstructed at approximately the correct

location, but since the problem is linearized, the quantitative values for μ_a are not exact. The reconstruction from the mean-time data showed a sharper reconstruction of the anomaly.

In cases 2 and 3, we showed the effects of the presence of a single smooth clear layer of 1- and 2-mm width, respectively. In both cases, we can see that even when the correct Jacobian is used for the reconstruction, the image of the anomaly is clearly affected by the presence of the clear gap, with the 2-mm-wide case showing the greatest effects. Furthermore, the presence of the clear gap causes the center of the anomaly to apparently move toward the inner boundary of the clear layer. This effect has been previously observed when using a nonlinear reconstruction algorithm.²⁰ When the Jacobian from the purely diffusing model is used to reconstruct images from clear-gap data, we see that the anomaly is apparently moved nearer to the center of the model, the effect again being most noticeable in the 2-mm-gap case. This effect has also been recently reported by other investigators using both simulated and measured data.²⁶

In the models where two nonscattering ventricles were also included, similar results to those obtained in cases 2 and 3 were seen. However, it seems that the presence of the ventricles in the 2-mm-gap case has rather paradoxically assisted the reconstruction algorithm, irrespective of whether the correct or the purely diffusing Jacobian was used. This is because the sensitivity of the reconstruction to the region in which the anomaly lies has been increased as a result of the presence of these void ventricles. This increase in sensitivity is, however, obtained at the cost of a loss in sensitivity deeper within the model, and had the anomaly been placed there, the effect of the ventricles on the reconstruction would have been to worsen its accuracy.

The effect of an irregular clear ring was also examined (case 4). The thickness of the clear ring varied between 0.5 and 2.5 mm, with a mean of 1.507 mm. Images of the internal μ_a distribution were reconstructed by using the Jacobian from the radiosity-diffusion model with knowledge of the nonscattering boundary position. Unlike images obtained for the smooth-surfaced models of equivalent average thickness, an image was reconstructed with relatively good quality.

In all of the above cases, we have shown that the linearized reconstruction may under certain circumstances be applied to models containing clear regions. We have presented here a quantitative study with the aim of a thorough explanation of the effects of clear regions in linear image reconstruction regardless of whether the correct inverse model is used. This work has shown that a major drawback is that the location of any void regions needs to be known *a priori* in order to facilitate correct localization of any μ_a changes within the domain. This is shown to be strongly the case where the model contains thick clear layers. However, it must be noted that when the data are measured from a domain that contains clear layers and/or ventricles, even though the use of a Jacobian from a purely diffusing model may produce an image identifying the presence of an anomaly, these anomalies may not necessarily be localized to the correct position.

Clinically, these results are significant with respect to

the accuracy of image reconstruction for neonatal studies. The data collected may be data measured over a period of time, where one expects a change in absorption due to either injury, treatment, or stimulus. The above study has illustrated that even though images of changes in absorption may be reconstructed from these data, regardless of the size and the location of the clear regions, these images will not accurately represent the actual location of the anomaly. Therefore if the only information needed is whether a change has occurred or not, this technique may be useful; however, if exact information regarding the position of any changes that have occurred in absorption is sought, addition of *a priori* knowledge will be crucial.

ACKNOWLEDGMENT

Funding has been generously received from the Engineering and Physical Sciences Research Council, UK.

Corresponding author H. Dehghani may be contacted by e-mail, hamid.dehghani@dartmouth.edu.

*Present address; Thayer School of Engineering, Dartmouth College, 8000 Cummings, Hanover, New Hampshire 03755-8000.

REFERENCES

1. J. C. Hebden, F. E. W. Schmidt, M. E. Fry, M. Schweiger, E. M. C. Hillman, D. T. Delpy, and S. R. Arridge, "Simultaneous reconstruction of absorption and scattering images by multichannel measurement of purely temporal data," *Opt. Lett.* **24**, 534–536 (1999).
2. B. W. Pogue, K. D. Paulsen, C. Abele, and H. Kaufman, "Calibration of near-infrared frequency-domain tissue spectroscopy for absolute absorption coefficient quantitation in neonatal head-simulating phantoms," *J. Biomed. Opt.* **5**, 185–193 (2000).
3. S. Fantini, M. A. Franceschini, E. Gratton, D. Hueber, W. Rosenfeld, D. Maulik, P. G. Stubblefield, and M. R. Stankovic, "Non-invasive optical mapping of the piglet in real time," *Opt. Express* **4**, 308–314 (1999).
4. H. Eda, I. Oda, Y. Ito, Y. Wada, Y. Oikawa, Y. Tsunazawa, Y. Tsuchiya, Y. Yamashita, M. Oda, A. Sassaroli, Y. Yamada, and M. Tamaru, "Multichannel time-resolved optical tomographic imaging system," *Rev. Sci. Instrum.* **70**, 3595–3602 (1999).
5. J. C. Schotland, "Continuous-wave diffusion imaging," *J. Opt. Soc. Am. A* **14**, 275–279 (1997).
6. J. C. Hebden, S. R. Arridge, and D. T. Delpy, "Optical imaging in medicine: I. Experimental techniques," *Phys. Med. Biol.* **42**, 825–840 (1997).
7. S. R. Arridge, "Topical review: optical tomography in medical imaging," *Inverse Probl.* **15**, R41–R93 (1999).
8. S. R. Arridge and J. C. Hebden, "Optical imaging in medicine: II. Modelling and reconstruction," *Phys. Med. Biol.* **42**, 841–853 (1997).
9. V. Ntziachristos and B. Chance, "Probing physiology and molecular function using optical imaging: applications to breast cancer," *Breast Cancer Res. Treatment* **3**, 41–46 (2001).
10. C. H. Schmitz, H. L. Graber, H. B. Luo, I. Arif, J. Hira, Y. L. Pei, A. Bluestone, S. Zhong, R. Andronica, I. Soller, N. Ramirez, S. L. S. Barbour, and R. L. Barbour, "Instrumentation and calibration protocol for imaging dynamic features in dense-scattering media by optical tomography," *Appl. Opt.* **39**, 6466–6486 (2000).
11. M. A. Franceschini, V. Toronov, M. E. Filiaci, E. Gratton,

- and S. Fantini, "On-line optical imaging of the human brain with 160-ms temporal resolution," *Opt. Express* **6**, 49–57 (2000), <http://www.opticsexpress.org>.
12. D. A. Boas, T. Gaudette, G. Strangman, X. F. Cheng, J. J. A. Marota, and J. B. Mandeville, "The accuracy of near infrared spectroscopy and imaging during focal changes in cerebral hemodynamics," *Neuroimage* **13**, 76–90 (2001).
 13. S. R. Arridge, M. Schweiger, M. Hiraoka, and D. T. Delpy, "A finite element approach for modeling photon transport in tissue," *Med. Phys.* **20**, 299–309 (1993).
 14. M. Schweiger, S. R. Arridge, M. Hiraoka, and D. T. Delpy, "The finite element model for the propagation of light in scattering media: boundary and source conditions," *Med. Phys.* **22**, 1779–1792 (1995).
 15. H. Jiang, K. D. Paulsen, U. L. Osterberg, B. W. Pogue, and M. S. Patterson, "Optical image reconstruction using frequency-domain data: simulations and experiments," *J. Opt. Soc. Am. A* **13**, 253–266 (1996).
 16. J. S. Wyatt, D. T. Delpy, M. Cope, S. Wray, and E. O. R. Reynolds, "Quantification of cerebral oxygenation and haemodynamics in sick newborn infants by near infrared spectroscopy," *Lancet* **ii**, 1063–1066 (1986).
 17. A. H. Hielscher, R. E. Alcouffe, and R. L. Barbour, "Comparison of finite-difference transport and diffusion calculations for photon migration in homogeneous and heterogeneous tissue," *Phys. Med. Biol.* **43**, 1285–1302 (1998).
 18. S. R. Arridge, H. Dehghani, M. Schweiger, and E. Okada, "The finite element model for the propagation of light in scattering media: a direct method for domains with non-scattering regions," *Med. Phys.* **27**, 252–264 (2000).
 19. J. Riley, H. Dehghani, M. Schweiger, S. R. Arridge, J. Ripoll, and M. Nieto-Vesperinas, "3D optical tomography in the presence of void regions," *Opt. Express* **7**, 462–467 (2000), <http://www.opticsexpress.org>.
 20. H. Dehghani, S. R. Arridge, M. Schweiger, and D. T. Delpy, "Optical tomography in the presence of void regions," *J. Opt. Soc. Am. A* **17**, 1659–1670 (2000).
 21. J. Ripoll, S. R. Arridge, H. Dehghani, and M. Nieto-Vesperinas, "Boundary conditions for light propagation in diffusive media with non-scattering regions," *J. Opt. Soc. Am. A* **17**, 1671–1681 (2000).
 22. J. Ripoll, M. Nieto-Vesperinas, and S. R. Arridge, "Effect of roughness in nondiffusive regions within diffusive media," *J. Opt. Soc. Am. A* **18**, 940–947 (2001).
 23. A. D. Klose and A. H. Hielscher, "Iterative reconstruction scheme for optical tomography based on the equation of radiative transfer," *Med. Phys.* **26**, 1698–1707 (1999).
 24. O. Dorn, "A transport-backtransport method for optical tomography," *Inverse Probl.* **14**, 1107–1130 (1998).
 25. M. Vauhkonen, "Electrical impedance tomography and *priori* information," Ph.D. dissertation (University of Kuopio, Kuopio, Finland, 1997).
 26. Y. Pei, H. L. Graber, and R. L. Barbour, "Normalized-constrained algorithm for minimizing inter-parameter crosstalk in DC optical tomography," *Opt. Express* **9**, 97–109 (2001), <http://www.opticsexpress.org>.
 27. M. Schweiger and S. R. Arridge, "Optimal data types in optical tomography," in *Information Processing in Medical Imaging (IPMI'97 Proceedings)*, Vol. 1230 of Lecture Notes in Computer Science, J. Duncan and G. Gindi, eds. (Springer-Verlag, Berlin, 1997).
 28. W. H. Press, S. A. Teukolsky, W. T. Vetterling, and B. P. Flannery, *Numerical Recipes in C*, 2nd ed. (Cambridge U. Press, Cambridge, UK, 1992).
 29. S. R. Arridge and M. Schweiger, "Photon-measurement density functions. Part 2: finite-element-method calculations," *Appl. Opt.* **34**, 8026–8037 (1995).
 30. M. Firbank, S. R. Arridge, M. Schweiger, and D. T. Delpy, "An investigation of light transport through scattering bodies with non-scattering regions," *Phys. Med. Biol.* **41**, 767–783 (1996).